Influence of Axial and Radial Diffusion Processes on the Analytical Performance of a Glow Discharge Cell

Mark van Straaten and Renaat Gijbels*

University of Antwerp, Department of Chemistry, Universiteitsplein 1, B-2610 Wilrijk, Belgium

Akos Vertes

George Washington University, Department of Chemistry, Washington, D.C. 20052

The concentration distribution of sputtered atoms in a glow discharge (GD) cell is calculated by numerically solving the mass transport equation in cylindrical coordinates. The obtained two-dimensional density map is used to estimate the diffusion current density toward different parts of the discharge cell. Back diffusion toward the sample surface determines the net etching rate of the sample and is found to be radially not uniform. As a result the profile of the crater bottom obtained by GD erosion is not flat but has a convex shape. A parametric evaluation of the discharge conditions regarding this convexity indicates a proportionality with the amount of material introduced into the plasma so that low discharge powers are to be preferred for the application of a glow discharge as a depth profiling device. Material transport to the sampling site can influence the sensitivity of an analytical glow discharge. It is shown that slight modifications of the boundaries of a GD cell can result in a more efficient sputtered neutral atom density distribution in the discharge cell.

INTRODUCTION

The use of glow discharge devices as excitation/ionization sources is growing rapidly in the field of analytical spectrometry. The simplicity of a glow discharge (GD) allows it to be coupled with various spectrometric detection systems: GD's have been successfully combined with optical emission (OES), mass (MS), and atomic absorption (AAS) spectrometers.[1] The choice of one of these analytical tools will depend on the application; a high sensitivity and selectivity are specific benefits of mass spectrometry. GDMS in the double-focusing configuration in particular has proven to be capable of sub-ppb detection limits[2] and is believed to be one of the most sensitive techniques for elemental analysis of solids. GDOES, although not as sensitive, has extensively been applied for chemical analysis of solid surfaces and thin film systems.[3,4]

Both GDOES and GDMS often make use of a discharge cell which constricts the discharge to a small volume. The understanding of the basic phenomena like atomization, excitation, ionization, and transport of sample material is essential for good analytical practice. The transport of sputtered material in a steady state GD-plasma is believed to be governed by a diffusion proces.[5,6] Ferreira et al.[6] determined the spatial distribution of sputtered atom concentrations in a GD by atomic absorption measurements and proposed a two-dimensional diffusion model to predict the atom number densities. The observed concentration profile showed a maximum close to the sample surface which could not be explained by their diffusion model. In a previous paper,[7] it was demonstrated that a one-dimensional diffusion profile can indeed exhibit such a maximum if the appropriate boundary conditions are applied. A continuation of this work is presented here and reports on the calculation of the two-dimensional distribution of sample atoms in a cylindrical glow discharge cell. With this distribution it is possible to estimate the amount of material transport to different parts of the cell which can influence its analytical performance. Different cell configurations are evaluated theoretically, regarding the depth profiling abilities and the sensitivity of a GD device.

DESCRIPTION AND MODELING OF A GLOW DISCHARGE

A glow discharge plasma in its simplest form is a planar electrode system embedded in a gas environment of reduced pressure (see Figure 1). Applying a high enough voltage across this electrode system will initiate the discharge and a plasma is formed in which different (up to 9[8]) zones can be distinguished. From the analytical standpoint only two of them are of interest: the cathode dark space (CDS) and the negative glow (NG). The former is a narrow zone just in front of the cathode which incorporates nearly the total potential drop across the discharge. Because it is the only region of the plasma where the (noble) gas ions can gain energy on their way to the cathode surface, it has high significance regarding sputtering: as a result of the bombardment of the cathode with accelerated ions and energetic neutrals formed by charge exchange collisions in the CDS, neutral cathode atoms are released. Ionization of these sputtered species (necessary for a mass spectrometric analysis) is negligible in the CDS[8] and takes place in the negative glow region mainly through electron impact and Penning ionization. This region takes up nearly the whole interelectrode space and is quasi-equipotential.

The sputtered species loose their initial energy of a few electron volts by collisions in the gas environment. After this thermalization process the transport of sputtered material is diffusion dominated: starting from an initial distribution of thermalized particles in the plasma, diffusion can take place toward and away from the cathode surface (which for analytical purposes is also the sample surface).

In a previous paper[7] it was shown that the CDS in a glow discharge can be modeled using a set of coupled Boltzmann transport equations to describe the flux energy distributions

* To whom correspondence should be addressed.

(1) Hess, K. R.; Marcus, R. K. *Spectroscopy* 1987, 2.

(2) Sanderson, N. E.; Hall, E.; Clark, J.; Charalambous, P.; Hall, D. *Mikrochim. Acta* 1987, *1*, 275.

(3) Ehrlich, G.; Stahlberg, U.; Hoffmann, V.; Scholze, H. *Spectrochim. Acta* 1991, *46B*, 115.

(4) Bengtson, A; Lundholm, M. *J. Anal. Atom. Spectrom.* 1988, *3*, 879.

(5) Van Dijk, C.; Smith, B. W.; Winefordner, J. D. *Spectrochim. Acta* 1982, *37B*, 759.

(6) Ferreira, N. P.; Human, H. G. C. *Spectrochim. Acta* 1980, *36B*, 215.

(7) van Straaten, M.; Vertes, A.; Gijbels, R. *Spectrochim. Acta* 1991, *46B*, 281.

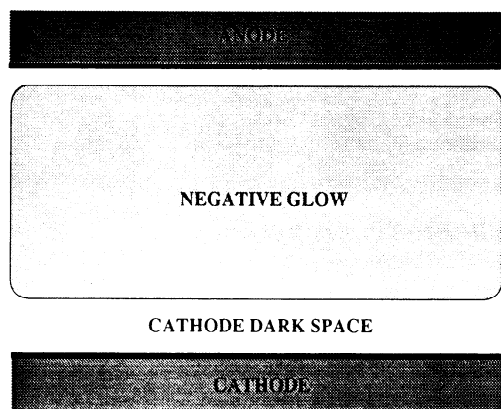(8) Chapman, B. *Glow Discharge processes*; Wiley: New York, 1980.

Figure 1. Schematic representation of a planar glow discharge.

Figure 2. Standard GD cell: (1) sample (cathode); (2) mask; (3) insulator; (4) cell body (anode); (5) gas inlet.

of the particles involved: ions, neutrals, and electrons.[9] The diffusion model was then addressed in one dimension yielding the concentration distribution of sputtered atoms on the axis of a planar glow discharge configuration. Here the solution of the diffusion problem in two dimensions is sought for a cylindrically symmetric glow discharge. As a result a two-dimensional concentration profile is obtained showing how the sputtered atoms are distributed in a certain discharge configuration.

Since we apply a GD as an atomization/ionization source for mass spectrometry in our laboratory, the standard discharge cell used for analyzing flat samples in a VG9000 instrument is taken as a starting geometry for the calculations.

MATHEMATICAL DIFFUSION MODEL

General. Once the sputtered sample atoms have lost their initial kinetic energy, the transport of material in a glow discharge plasma can be regarded as a diffusion process. The time-dependent variation of the number density of sputtered particles can then be described by the mass transport equation[10]

$$\frac{\partial n(x,y,z)}{\partial t} = D\nabla^2 n(x,y,z) - [\text{sink}] + [\text{source}] \qquad (1)$$

where we assume that the diffusion coefficient, D, is constant throughout the plasma. The sink and source terms on the right-hand side of eq 1 account for removal and production fluxes of material, respectively. Since most GD systems have cylindrical symmetry, it is useful to transform eq 1 into cylindrical coordinates:

$$\frac{\partial n(r,z)}{\partial t} = D\left[\frac{\partial^2 n(r,z)}{\partial r^2} + \frac{1}{r}\frac{\partial n(r,z)}{\partial r} + \frac{\partial^2 n(r,z)}{\partial z^2}\right] - [\text{sink}] +$$
$$[\text{source}] \quad (2)$$

The removal of sputtered particles in the system under study (Figure 2) is mainly caused by deposition on the surrounding walls and by the gas flow through the cell exit slit. Deposition is accurately dealt with using the appropriate boundary conditions for eq 2; the convective flow of particles can be described by the sink term[10]

$$[\text{sink}] = \bar{v}(r,z)\bar{\nabla}n(r,z) \qquad (3)$$

with $\bar{v}(r,z)$ being the flow (convection) velocity of the sputtered neutrals. This velocity and its distribution is not known but can be taken as equal to the axial gas flow velocity which can be estimated from the gas volume flow through the exit slit.[6] The relative importance of such a sink term is investigated by Ferreira et al.[6] They pointed out that the gas flow velocity
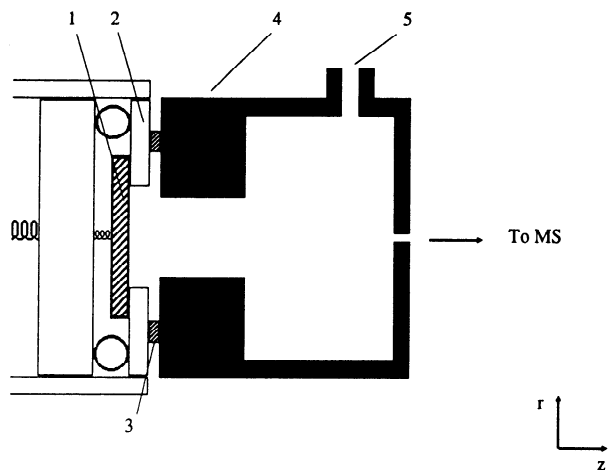
is small compared to the thermal velocity of the sputtered atoms and that it therefore has no significant influence on the distribution $n(r,z)$. Since we are interested merely in the more qualitative aspects, we have chosen to neglect this sink term. The production of particles, however, has to be accounted for. In our description of the diffusion model this is not done by using a boundary condition which equates the sputter rate of the sample to the net flux of particles into the plasma, as is formulated by Ferreira et al. Instead a certain thermalization profile is assumed to exist,[11] giving the initial spatial dependence of the sputtered particles when they have lost their kinetic energy after a number of collisions in the gas environment. This fundamental difference makes it possible to have also diffusion toward the sample surface and not only away from the sample as is suggested in ref 6. The source term can then be expressed as

$$[\text{source}] = J_0 F_{\text{T}}(r,z) \qquad (4)$$

where $F_{\text{T}}(r,z)$ gives the normalized spatial dependence of a sputtered particle after being thermalized and J_0 corresponds to the sputter flux (number of atoms/cm^2 s released into the plasma by the sputter process).

If a steady state is reached, there is no temporal variation in the atom number density and eq 2 simplifies to

$$D\left[\frac{\partial^2 n(r,z)}{\partial r^2} + \frac{1}{r}\frac{\partial n(r,z)}{\partial r} + \frac{\partial^2 n(r,z)}{\partial z^2}\right] + J_0 F_{\text{T}}(r,z) = 0 \quad (5)$$

Input Quantities. (1) Diffusion Coefficient, D. The diffusion coefficient in a binary system according to the rigid sphere model can be calculated from[12]

$$D = K\frac{\sqrt{T^3(M_s + M_g)/2M_sM_g}}{pd_{sg}} \qquad (6)$$

where T is the temperature (K), M_g and M_s are the atomic masses of the gas and sputtered solid (amu), p is the pressure (Pa), and $d_{sg} = (d_s + d_g)/2$ with d_s and d_g being the atomic diameter of the colliding species (cm). K is a numerical constant.

A further correction to the binary diffusion coefficient is possible using other interaction models for the diffusing particles but seemed unnecessary in the scope of the calculations (deviations of ca. 10%). Table I gives the calculated diffusion coefficient in a Mo/Ar system for three different pressure regimes.

(9) Abril, I. Comput. Phys. Commun. 1988, 51, 413.
(10) Hershey, D. Transport Analysis; Plenum Press: New York, 1973.

(11) Valles-Abarca, J. A.; Gras-Marti, A. J. Appl. Phys. 1984, 55, 1370.
(12) Hirschfelder, J. O.; Curtiss, C. F.; Bird, R. B. Molecular Theory of Gases and Liquids; John Wiley: New York, 1954.

Table I. Discharge Conditions (p, I, V) and Input Parameters for the Transport Equation

p (Pa)	I (mA/cm^2), V	D (cm^2/s)	T (K)	J_0 (at/cm^2 s)
50	0.96, 881	1714	325	0.875×10^{16}
	1.81, 1004	1714	325	2.209×10^{16}
	2.91, 1203	1714	325	4.631×10^{16}
75	1.66, 688	1286	325	1.028×10^{16}
	3.53, 881	1286	325	3.609×10^{16}
	4.72, 1069	1286	325	6.633×10^{16}
100	1.76, 682	857	325	0.886×10^{16}
	3.14, 747	857	325	2.202×10^{16}
	5.29, 962	857	325	5.781×10^{16}
	7.94, 1205	857	325	12.043×10^{16}

(2) *Thermalization Profile, $F_T(r,z)$.* As a result of noble gas sputtering, neutral atoms are released from the sample target having initial energies of a few electron volts. The angular and energetic spectrum of this flux can be described by[11,13]

$$\Phi(E,\theta) = 2UE(E + U)^{-3} \cos \theta/\pi \qquad (7)$$

where U is the surface binding energy of the target (usually taken equal to the sublimation energy) and θ is the angle which the initial trajectory of the sputtered particle makes with the source normal. Due to multiple collisions with the atoms of the surrounding gas environment, these sputtered particles will loose their kinetic energy and have only thermal energy. To describe the spatial profile of stopped (thermalized) particles, one can define the distribution $F(E,\theta,z)$, so that $F(E,\theta,z)$ dz is the probability that a particle which had initial energy E and direction θ with the source normal is stopped in the gas layer $(z, z + dz)$. At this moment we assume that the sample surface and the gas environment are infinite, so that there is no radial dependence $(F(E,\theta,r,z) = F(E,\theta,z))$. In order to come to the spatial distribution of thermalized particles, the distribution of interest is then $F_T(z)$, the convolution of $F(E,\theta,z)$ with the energetic and angular spectrum of the particle flux emitted by the sputter target[11]

$$F_T(z) = \int \int dE \, d\Omega \, \Phi(E,\theta)F(E,\theta,z) \qquad (8)$$

The distribution function $F(E,\theta,z)$ can be calculated by taking into account the different collisional events which lead to an energy loss of the sputtered neutral. In general, two processes have to be considered:

(A) Elastic collisions between the energetic neutral atom and a gas atom in which the neutral transfers a certain amount of energy T_n to the nucleus of the gas atom target. This event can be combined with a change in direction (scattering) of the particle slowing down and is determined by the nuclear scattering cross section $\sigma_n(E,T_n,\theta,\theta')$, indicating that the state of the neutral atom changes from (E,θ) to $(E - T_n,\theta')$.

(B) Inelastic collisions in which the energy loss of the energetic neutral is transferred to the electrons of the colliding gas atom. This event is characterized by the inelastic (electronic) cross section σ_e (E,T_e,θ) and an energy loss T_e. These kinds of collisions do not bring about a change in direction of the neutral.

The next step is to calculate the distribution function $F(E,\theta,z)$ and solve the convolution integral, eq 8. This is done in the appendix using a continuous slowing down approximation, where scattering and inelastic collisions are neglected. The distribution of thermalized sputtered particles then becomes

$$F_T(z) = \frac{R_U/z}{(1 + (R_U/z)^2)^2} \qquad (9)$$

where R_U corresponds to the range of particles with energy

U, the surface binding energy of the target (see appendix).

(3) *Sputtered Particle Flux, J_0.* The flux of material released under the sputter action of the noble gas (atoms/cm^2 s) is estimated using a mathematical computer code which models a one-dimensional planar glow discharge.[9] In a previous paper[7] this model has been checked by comparing experimental and calculated etching rates for a Mo/Ar system, incorporating a fitting parameter to reach agreement between calculated and experimental etching rates. Since the treatment was one-dimensional, this parameter was believed to account for the radial diffusion processes in the discharge cell. The present description of a two-dimensional diffusion process should result in a parameter-less agreement.

The sputter flux, J_0, is obtained by calculating the sputter yield of the cathode target in a glow discharge due to ion and atom bombardment utilizing the ion and neutral flux energy distributions at the cathode surface ($f_i(z,E)$ for $z = 0$), and an empirical formula[14] for the sputtering yield, $Y(E)$

$$J_0 = \int dE \, Y(E)[f_{ion}(z,E) + f_{neutr}(z,E)] \qquad (10)$$

The computer code calculates the flux energy distributions $f_i(z,E)$ by solving a set of coupled Boltzmann transport equations for ions, neutrals, and electrons describing the main processes in the dark space of a glow discharge (charge exchange, ionization, and secondary electron emission by the target). Further details on this are found in ref 9. Table I gives the values, as calculated, for J_0 in the Mo/Ar system at three different pressures and power densities, corresponding to the experimental conditions at which the etching rate was also measured.[7]

Solution of the Diffusion Equation. The partial differential equation described in eq 5 can be approached analytically as long as the boundary of the two-dimensional region where the function $n(r,z)$ is to be determined is relatively simple. For more complex systems, like the one under study, one has to use numerical methods. With the particular boundaries determined by the walls of the discharge cell and with the specific boundary conditions, eq 5 is solved using a computer program EPDE1,[15] based on a finite difference method. The essence of the method is to superimpose upon the region of interest a net and to replace the partial differential equation to be solved by an approximate difference equation at each nodal point of the net. The value of the function of interest, $n(r,z)$, at a certain nodal point of the domain is then calculated according to its neighboring points and starting from a "guess" for all not boundary points. The solution is then found by the method of successive overrelaxation, an iterative scheme with a correction process which is applied until the values of the function $n(r,z)$ are jugded to be sufficiently close to the "true solution". This method of solving partial differential equations also allows boundary conditions involving a derivative of the unknown function. Since the system under consideration has cylindrical symmetry, this applies for the z-axis of the system, as can be seen from Figure 2. On the z-axis, which coincides with the axis of the glow discharge cell, a condition of the form $D\partial n(0,z)/\partial r = 0$ is valid, indicating that there is only an axial and no radial diffusion flux on the cel axis.

Solving eq 5 numerically has the advantage that it allows fairly complex boundaries; in that way different cell designs can be investigated upon analytical performance. For all investigated cell designs the following boundary conditions apply:

(13) Thompson, M. W. *Philos. Mag.* **1968**, *18*, 377.

(14) Yamamura, Y.; Matsunami, N.; Itoh, N. *Radiat. Eff.* **1983**, *71*, 65.
(15) Hornsby, J. *EPDE1*; CERN Computer Centre Program Library D300, Geneva, 1977.

$$n(r,z) = 0 \quad \text{on all cell walls}$$

$$\frac{\partial n(0,z)}{\partial r} = 0 \quad \text{on the cell axis} \tag{11}$$

$$J_0 F_T(z) = 0 \quad \text{for } r > R$$

where R is the radius of the crater in the sample surface formed by the sputter action of the plasma. In the preceding section on the thermalization profile, it was silently assumed that the thermalization and diffusion processes are decoupled. Since the distance traveled (by a sputtered particle) by diffusion in the lapse of time of the slowing down process is one order of magnitude smaller than the mean range of the particles, thermalization can be regarded as an instantaneous process and decoupling from the diffusion process is justified.[11]

RESULTS AND DISCUSSION

For the standard cell design, depicted in Figure 2, the calculated spatial variation of the molybdenum sputtered atom concentration in an argon discharge is shown in Figure 3 for a typical set of discharge conditions. Since the distribution is not uniform, material fluxes in different directions occur. From an analytical standpoint, diffusional transport of material can then determine the performance of a GD cell. In the case of GDMS, the ions are sampled close to the exit slit at the back of the cell so that a high concentration of sputtered atoms at the exit slit as well as a large (axial) diffusion flux toward the exit slit are preferable from a sensitivity point of view. GD's are also used for depth profiling (combined with OES or MS), and in this case the possible mass transport toward the sample surface can influence the depth resolution. Both diffusional fluxes can be estimated from the calculated concentration distribution in the GD cell obtained by solving eq 5. Different cell designs can then be investigated upon analytical performance merely by changing the boundaries of the investigated system.

Calculated Crater Profiles and Etching Rate. As can be seen from Figure 3, the concentration profile exhibits a maximum close to the sample surface, a result of the decoupling of the thermalization process from the diffusion process. Consequently, the diffusion flux of sputtered material toward the sample surface is nonzero and can be estimated from the slope of the concentration distribution near the sample surface

$$J_{\text{diff}} = -D\left(\frac{\partial n}{\partial z}\right)_{z=0} \tag{12}$$

J_{diff} then corresponds to the number of atoms/cm^2 s returning to the sample surface by diffusion. Since the sputter flux is known, the net etching rate (E, cm/s) of the sample can be calculated:

$$E = J_{\text{net}}\frac{M_s}{N_A \rho_s} \tag{13}$$

$$J_{\text{net}} = J_0 - J_{\text{diff}} \tag{14}$$

where J_0 is zero outside the crater surface (the size of which is determined by the cell structure). M_s and ρ_s correspond to the atomic weight and the density of the sample material, respectively, and N_A is Avogadro's number. A typical calculated crater profile in a Mo sample obtained after 1 h sputtering in an Ar discharge ($p = 75$ Pa, $V = 881$ V, $I = 3.53$ mA/cm^2) is shown in Figure 4. From this figure two features of GD etching can be seen. First, the crater profile displays a large rim at the crater edge. This is caused by the fact that back diffusion also occurs outside the crater, although no material is sputtered away here. J_{net} (eq 14) then becomes
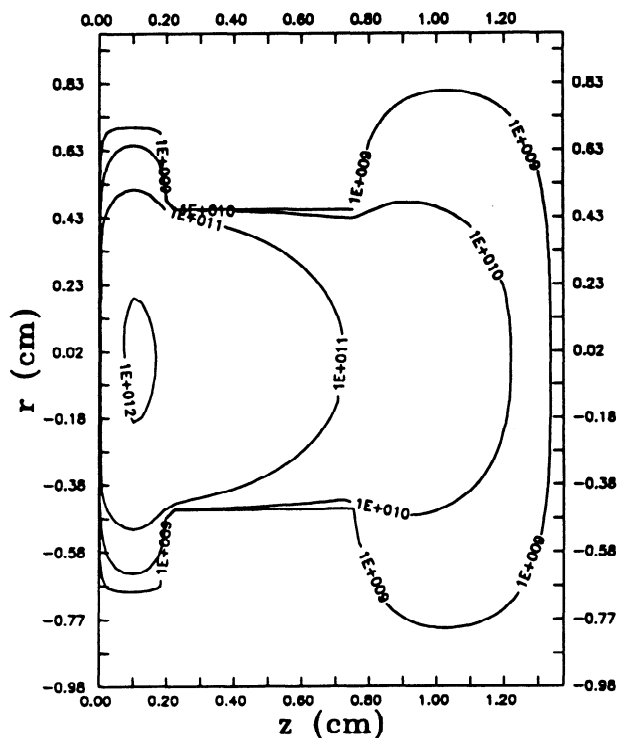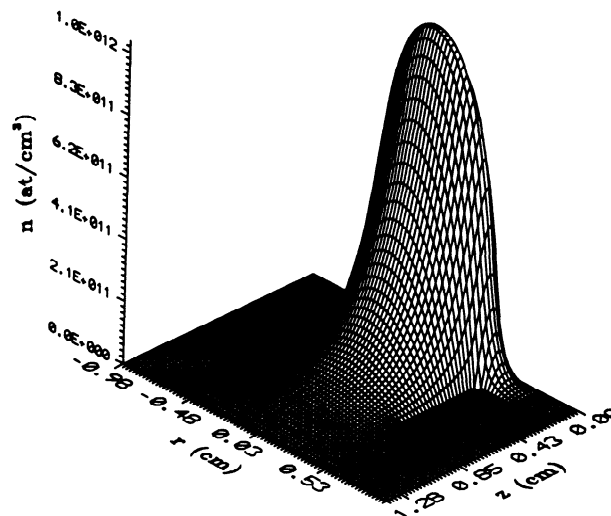

Figure 3. (a, Top) Density map for the sputtered neutral Mo atoms in a Mo/Ar glow discharge system ($p = 75$ Pa, $I = 3.53$ mA/cm2, $V = 881$ V). (b, Bottom) Topographic representation of the concentration distribution of sputtered Mo atoms in a Mo/Ar GD system ($p = 75$ Pa, $I = 3.53$ mA/cm^2, $V = 881$ V, cross section of part a through the r,z plane).

negative, yielding a negative etching rate, indicating material accumulation on the sample surface. The existence of a concentration gradient causing the back diffusion outside the crater is the result of incorporating the possibility of radial diffusion in the model. Second, the crater bottom is not flat, but has a convex shape. Because J_0 is constant over the whole crater surface, this means that J_{diff} is a function of the radial distance, r, a result of nonuniform radial mass transport. This crater shape is observed by several authors. Nickel et al.[16] showed comparable crater profiles and pointed out the influence of the bottom shape on the depth resolution. Data provided by ref 17 indicate a convex crater shape, although exact profiles were not shown. Up until now this convexity

(16) Nickel, H.; Guntur, D.; Mazurkiewicz, M.; Naoumidis, A. *Spectrochim. Acta* **1991**, *46B*, 125.

(17) Jährling, R. *Tagungsbericht 3. Anwendertreffen Analytische Glimmentladungs-Spectroskopie*; Konferenzen des Forschungscentrum Jülich, 1990, Band 2, p 83.
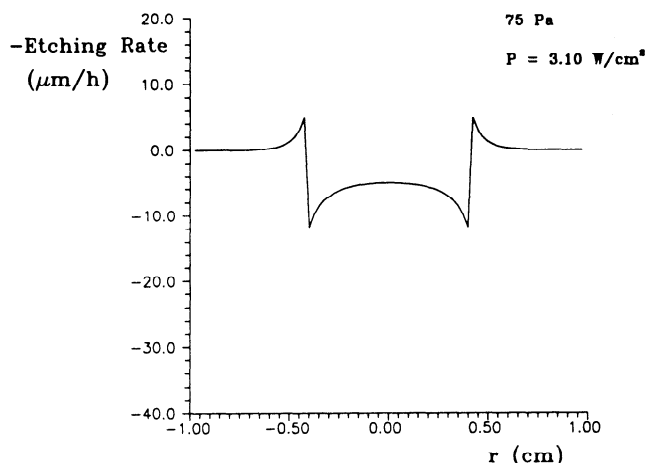
Figure 4. Theoretical crater profile in a Mo sample after 1-h exposure to an Ar GD-plasma (p = 75 Pa, I = 3.53 mA/cm^2, V = 881 V).
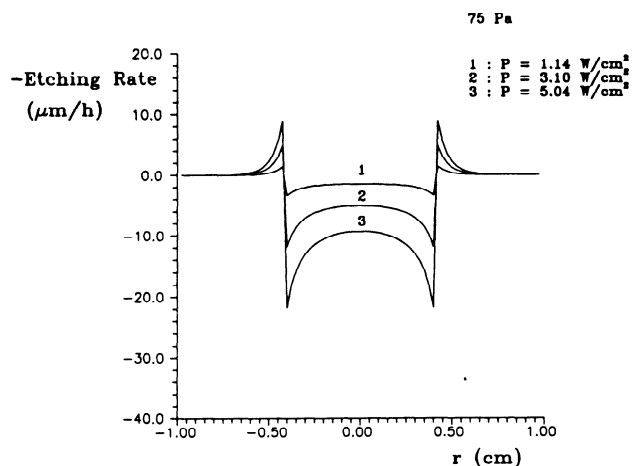

Figure 5. Theoretical crater profiles in a Mo sample after 1-h exposure to an Ar GD-plasma for three different power densities.

Figure 6. Calculated information thickness as a function of power density for three different pressures (Mo/Ar system).

Figure 7. Theoretical depth profile for a layered sample (A, B). Solid lines, standard cell; dashed lines, partial shielding of the sample surface. Discharge conditions: p = 75 Pa, I = 3.53 mA/cm^2, V = 881 V.

was explained by a nonuniform cathode dark space in front of the sample surface, the part of the plasma in a GD which incorporates the total voltage drop across the discharge. Consequently, the energy gained by the sputtering particles is not uniform, and since the sputtering yield is dependent on energy, this may cause a nonuniform etching rate. Here we show that nonuniform radial mass transport, combined with a uniform dark space, could be an alternative explanation.

It is obvious that the sputtered particle flux, J_0, and the back diffusion particle current density J_{diff} are dependent on the discharge conditions, thus affecting the net etching rate of the sample. Equation 5 is solved for the different discharge conditions mentioned in Table I, and the etching rates are calculated. The plasma characteristics chosen for the calculations are those for which the etching rate was also measured experimentally and reported in a previous paper.[7] For a given pressure (75 Pa) the calculated crater profiles in a Mo sample after 1-h exposure to an Ar plasma are shown in Figure 5 at three different power densities. As can be seen from this figure, the convexity of the crater bottom increases with power density, and consequently also the information thickness (defined as the maximum minus minimum crater depth) because at a given time the analyte originates from different depths in the sample, indicating that lower discharge conditions are preferable for obtaining flatter crater bottoms. Examining the source term in the diffusion equation (eq 5) more closely, it can be noticed that for a given pressure $F_T(z)$ and D are constant ($F_T(z)$ is a normalized distribution function which is only pressure dependent) so that by changing the discharge power only I is altered. This means then that J_0
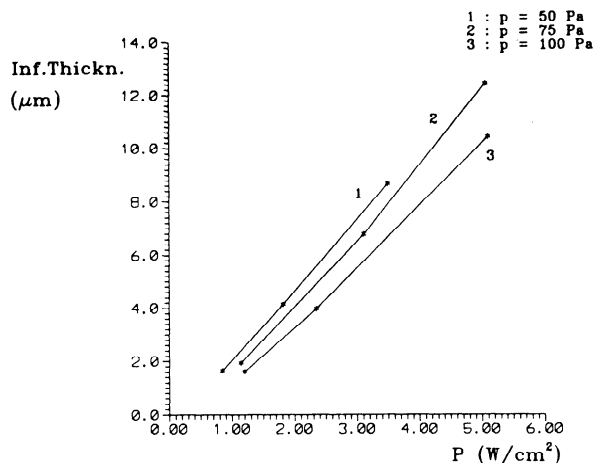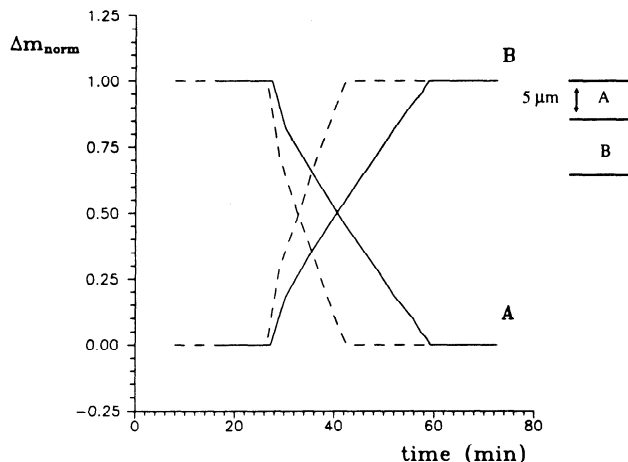
influences the radial distribution of the back diffusion current density, J_{diff}. A flat crater bottom would indicate that the radial diffusion current density is constant or zero (no radial concentration gradient), a condition which is in this description only met on the cell axis. Increasing the input of material induces larger and nonuniform radial concentration gradients so that the axial diffusion current density toward the sample surface is not constant over the whole crater surface and a more convex crater shape is obtained. Figure 6 shows the dependency of the information thickness on discharge power for three pressures. For a constant power density the information depth is inversely proportional to the pressure because lower pressures yield higher sputter fluxes.

It is interesting to investigate the effect of these crater profiles on the theoretical depth profile of a layered sample. Suppose a sample with a layered structure as shown in the right upper corner of Figure 7 is analyzed as a function of time with a GD device. Assuming that material A and B have equal sputter rates (J_{0A} = J_{0B}), the material loss at different time intervals can be calculated as a function of the radial distance, r. The theoretical depth profile for a specific set of discharge conditions is presented in Figure 7, assuming that the amount of material liberated in the plasma gives rise to a proportional analytic signal intensity (solid lines). Because of the convexity of the crater bottom, the measured signal as a function of time will change from a step function like behavior (for an infinite depth resolution) to a more smeared out signal. The value of the slope of the increasing/decreasing signal in the interface region indicates to what
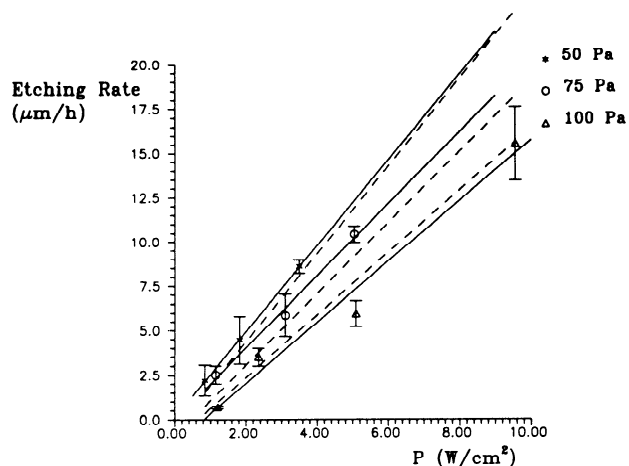
Figure 8. Measured and theoretically calculated etching rates for the Mo/Ar GD system as a function of power density for three different pressures.

Figure 9. Theoretical crater profiles in a Mo sample after 1-h exposure to a GD-plasma: (1) standard cell configuration; (2) partial shielding of the sample. Discharge conditions: p = 75 Pa, I = 3.53 mA/cm^2, V = 881 V.

extent the depth resolution is deteroriated. In this specific case the depth resolution is about 2.5 μm (83-17% definition[18]).

It is now possible to examine how the theoretical etching rates compare to experimental data. Figure 8 demonstrates the correlation between the etching rate and the power density at three pressures. The dashed lines correspond to the best fit for the theoretical etching rates at each pressure (the mean etching rate over the whole crater surface is taken); the solid lines give the best fits through the experimental points. As can be seen from the figure, the agreement between experiment and theory is satisfactory. In a previous paper we mentioned a similar agreement for a one-dimensional treatment of the diffusion problem. The fitting parameter needed in that model was believed to account for radial diffusion processes. In the two-dimensional view elaborated here, no fitting parameter is neccessary, justifying its introduction and interpretation in the one-dimensional case.

Although several authors have reported comparable experimental crater profiles as the ones calculated here, our experimental data did not back up this convexity in all cases. Several reasons can account for this inconsistency. The experimental crater profiles shown in ref 7 did not unambiguously reveal a convex crater bottom of the proportions as calculated here. The initial sample surface was occasionally bent, resulting in a crater pit superimposed on a curved surface which made the assessment of the depth and the crater profile sometimes rather difficult. This initial bending was caused by the sample cutting and polishing prior to plasma exposure; the error bars on the experimental points in Figure 8 reflect these experimental difficulties. Secondly, most of the experimental crater profiles reported in the literature stem from GD-optical studies. For GD-OES, higher gas pressures and discharge currents are used, giving higher sputter yields. Since the crater bottom profile is determined by the amount of back diffusion and its radial distribution, a more convex crater shape is then anticipated at these discharge conditions. The fact that those are not as pronounced as observed at lower discharge pressures[7] might suggest that the value for J_{diff} is overestimated or that its dependence on the radial distance, r, is not so critical. The former statement implies, however, that the sputter particle flux, J_0, is also too large, otherwise the estimated etching rates (as calculated from the net flux of material, see eq 13) would not yield comparable values to the experimental data. At this point it is not yet fully clear what causes this inconsistency. A more unambiguous ex-
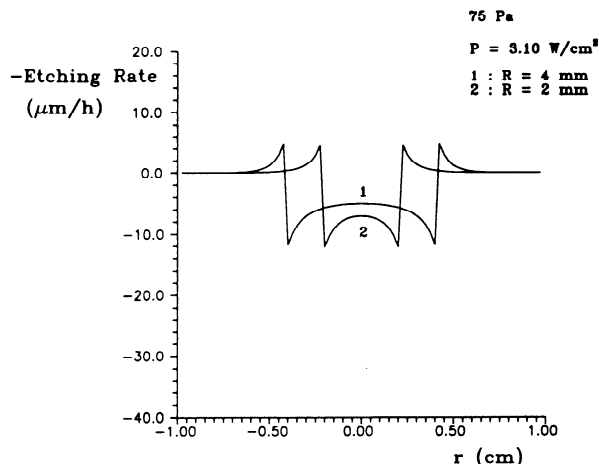
perimental determination of crater profiles at various discharge conditions is currently being set up to obtain more reliable data of the experimental crater profile under various discharge conditions. Still we can conclude that the radial nonuniform redeposition is the mean cause of a rather large information thickness in GD systems and we start from this fact to try to find a modified cell configuration which leads to an improvement in depth resolution.

One way of diminishing the convexity of the crater bottom is simply to allow less material to be introduced into the system, thus decreasing the concentration gradients inside the discharge cell. Supposing that the analytical tool to observe the sputtered material (OES or MS) is sensitive enough, this can easily be achieved by reducing the discharge conditions as is already mentioned. Another way of doing so is a partial shielding of the sample surface with a mask. As a result less material is put into the plasma, but at the same time the etching rate of the sample stays high. An example of a resulting crater profile where the exposed surface area is reduced by a factor of 4 is presented in Figure 9 together with the crater profile for the standard configuration obtained for the same set of discharge conditions. It is obvious that the information thickness is confined between narrower limits so that a better depth resolution can be expected. Again the theoretical depth profile for a layered sample can be calculated; in Figure 7 the result is shown by the dashed curves: the depth resolution is now estimated at 1.6 μm, compared to 2.5 μm for the standard cell configuration.

Cell Design and Sensitivity. Up until now we have examined the effect of the back diffusion particle current density on the crater shape in the sample surface, starting from a certain cell geometry (Figure 2). The cell geometry also has, however, an influence on how the sputtered particles are distributed in the cell. In order to optimize the sensitivity of the analytical method, one wants to have the highest possible concentration of analyte species (atoms, ions) near the sampling region. In our case where the GD is employed as an atomization/ionization source for mass spectrometry, most of the extracted and analyzed ions originate from close to the exit slit so that a high concentration of ions in this region is preferable.

The standard cell used in our mass spectrometer for analyzing flat samples has a "neck"-formed anode body to constrict the discharge to a part of the sample surface. This neck in the anode body is a necessary evil: it constricts the discharge but also prevents the sputtered material from spreading efficiently further on in the cell, since a large part will be deposited on the neck walls. The axial density profile
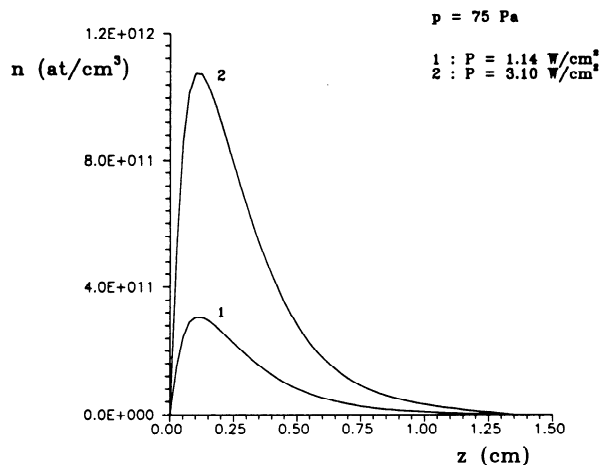
(18) Oechsner, H., Ed. *Thin Film and Depth Profile Analysis*; Springer-Verlag: Berlin, 1984.

Figure 10. Calculated axial ($r = 0$) density profile for Mo atoms in the standard GD cell for two different power densities ($p = 75$ Pa).

of sputtered neutrals for two discharge powers (Mo/Ar system, 75 Pa) as it is obtained from a cross section of Figure 3 through the symmetry axis ($r = 0$) of the system is shown in Figure 10. The profiles exhibit a maximum close to the sample surface, a consequence of implementing the thermalization profile of sputtered particles as a source term in the diffusion model and thus allowing back diffusion to the sample surface.

Our treatment of the diffusion problem makes it possible to change the boundaries of the cell so that we are able to investigate whether slight modifications in cell configuration will improve the distribution of the atoms. Since a lot of material is deposited on the neck of the cell, an improvement can be made by cutting off a part of the neck (Figure 11a), thus making a widespread distribution of sputtered atoms toward the end of the cell easier. A topographic presentation of the concentration distribution in such a cell configuration is demonstrated in Figure 11b. Regarding a high concentration of sputtered species near the exit slit, it would be even more advantageous to have no neck in the cell at all. But then the discharge is no longer constricted to the sample surface, and the shielding mask is also eroded by the plasma. To avoid this, one can make the mask part of the anode body and place the insulating ring behind the mask (Figure 12a). Then the mask itself constricts the discharge, and the axial material transport to the end of the cell is improved because deposition in the first part of the cell is avoided and at the same time more sputtered material is allowed to be introduced into the cell due to its increased volume. The latter is the result of assuming a steady-state plasma ($dn/dt = 0$): the larger the volume in which a steady concentration and distribution has to be reached, the more material is required to be put into the system. Figure 12b shows the concentration distribution of the sputtered neutrals for this cell. If we make a cross section along the z-axis ($r = 0$) through the two modified configurations investigated, it is clear that the concentration profiles show an increase of sputtered atom density near the exit slit of the modified cell compared to the distribution in the standard cell, as is shown in Figure 13. Also the diffusion flux on the cell axis increases, which can be estimated from the slope of the diffusion profile close to the exit slit

$$J_{\text{diff}} = -D\left(\frac{\partial n}{\partial z}\right)_{z=z_{\text{max}}; r=0} \tag{15}$$

For the cell without the neck a 3 times higher axial diffusion flux is obtained. With the boundary conditions applied here ($n = 0$ on the cell walls), J_{diff} is of course directly proportional with the atom number density. Since J_{diff} corresponds to a number of atoms crossing an imaginary plane of 1 cm²/s, a larger diffusion flux indicates that more material is trans-
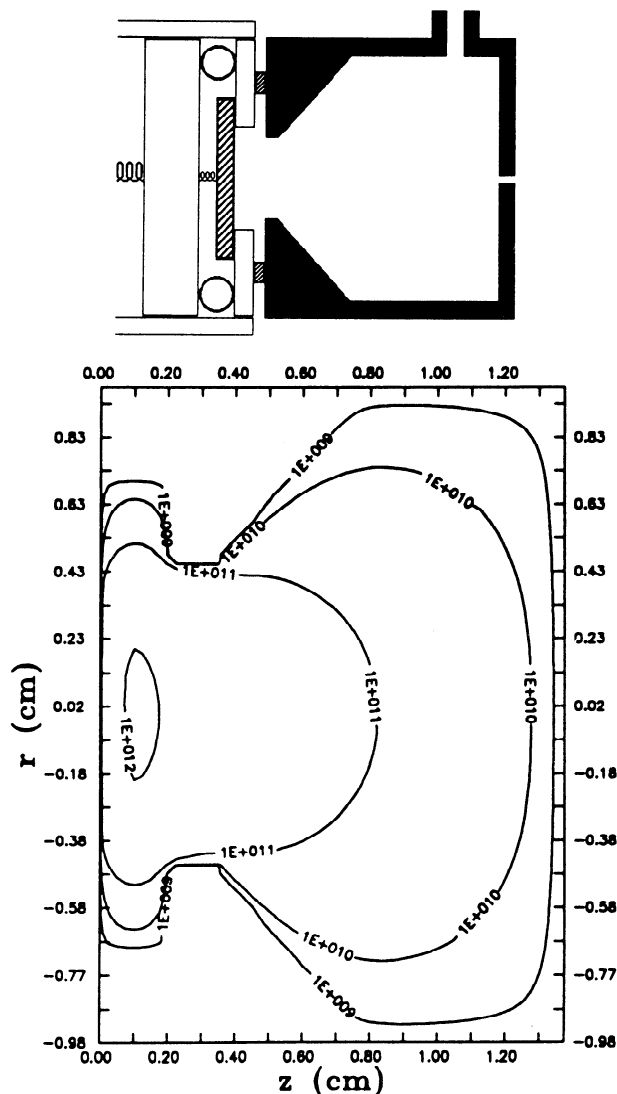

Figure 11. (a, Top) Modified cell configuration in which a part of the neck is cut off. (b, Bottom) Topographic representation of the concentration distribution of sputtered Mo atoms in a Mo/Ar GD system for the modified cell shown in part a ($p = 75$ Pa, $I = 3.53$ mA/cm², $V = 881$ V).

ported to the region of analytical interest. Although the present calculations deal with atoms only and a constant ionization efficiency throughout the cell is assumed for GDMS (which is certainly not the case), it is not probable that the ionization efficiency will change considerably in the modified cell configuration. Therefore, it can be expected that a relative increase in atom number density will yield a corresponding increase in ion density.

In Figure 13 a part of the calculated density profile for a higher discharge power in the standard cell is shown by the dashed curve. This indicates that the improved cell even brings about a higher neutral atom density and diffusion flux near the exit slit for a lower discharge power because of a more efficient sputtered neutral distribution in the cell.

It should be noticed that a comparable cell as the one described here is currently developed by VG to achieve a more sensitive analysis for flat sample forms with the VG9000 mass spectrometer. The theoretical evaluation of this cell design given here can be seen as an a posteriori explanation of the expected higher sensitivity. An experimental survey of the analytical capabilities of this new cell is currently underway and will be reported in the near future.
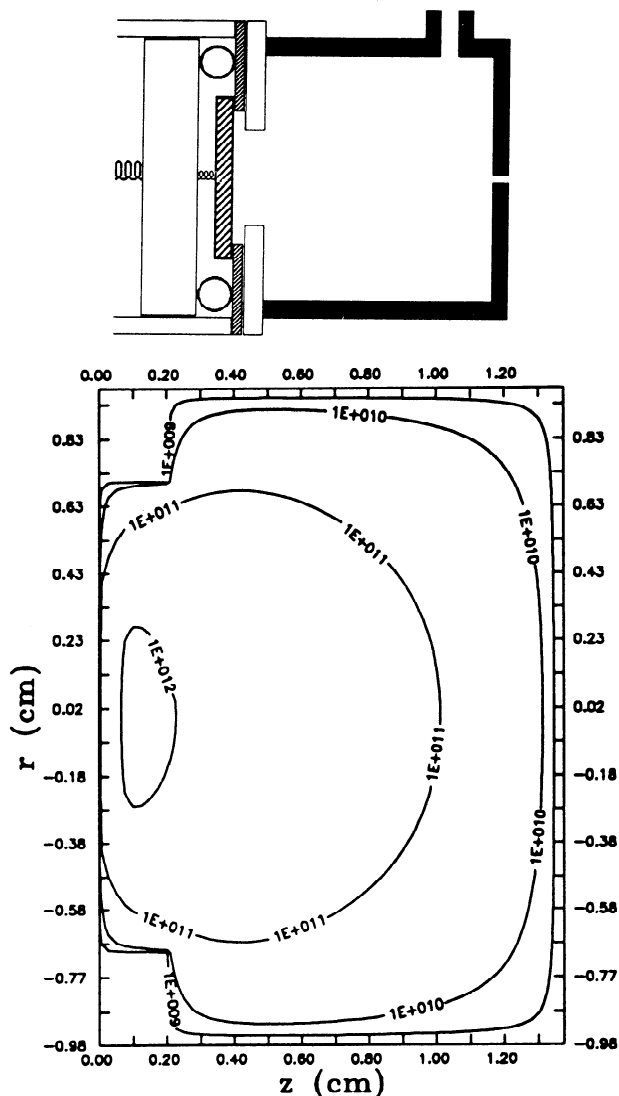
Figure 12. (a, Top) Modified cell configuration in which the shielding mask forms a part of the anode body. (b, Bottom) Topographic representation of the concentration distribution of sputtered Mo atoms in a Mo/Ar GD system for the modified cell shown in part a ($p = 75$ Pa, $I = 3.53$ mA/cm^2, $V = 881$ V).

Figure 13. Calculated axial ($r = 0$) density profiles for Mo atoms in the three cells investigated: (1) standard cell; (2) cell depicted in Figure 11a; (3) cell depicted in Figure 12a (discharge conditions for 1, 2, and 3: $p = 75$ Pa, $I = 3.53$ mA/cm^2, $V = 881$ V); (4) standard cell with higher discharge power applied ($p = 75$ Pa, $I = 4.72$ mA/cm^2, $V = 1069$ V).

cation: avoiding the use of a "neck"-formed anode body to constrict the discharge to the sample surface yields a higher concentration and diffusional mass transport to the region of analytical interest.

APPENDIX

Consider a gas layer of width Δz in front of the sample surface. If $\Delta z N/\cos \theta \, d\sigma_j$ is the probability of a collision in the gas layer, with N being the number density of the gas, resulting in an energy loss between T_j and $T_j + dT_j$ ($T_j = T_e$ or T_n), the distribution function at $z > \Delta z$ can be written as

$$F(E,\theta,z) = \frac{\Delta z N}{\cos \theta} \int d\sigma_j \, F(E - T_j, \theta_j, z - \Delta z) +$$

$$\left(1 - \frac{\Delta z N}{\cos \theta} \int d\sigma_j\right) F(E,\theta,z - \Delta z) \quad (A1)$$

where θ_j equals θ' for an elastic collision and θ for an inelastic collision. The first term on the right-hand side accounts for those particles which have undergone a collision, the second term for those which emerge from the layer without scattering or energy loss. Since $d\sigma_n$ and $d\sigma_e$ are completely separable, eq A1 becomes

$$F(E,\theta,z) =$$

$$\frac{\Delta z N}{\cos \theta} [\int d\sigma_n F(E - T_n, \theta', z - \Delta z) + \int d\sigma_e F(E - T_e, \theta, z - \Delta z)] +$$

$$\left[1 - \frac{\Delta z N}{\cos \theta} (\int d\sigma_n + \int d\sigma_e)\right] F(E,\theta,z - \Delta z) \quad (A2)$$

Expanding $F(E - T_i, \theta_i, z - \Delta z)$ up to the first order in Δz yields

$$F(E,\theta,z) =$$

$$\frac{\Delta z N}{\cos \theta}\left[\int d\sigma_n\left[F(E - T_n, \theta', z) - \Delta z \frac{\partial F(E - T_n, \theta', z)}{\partial z}\right] +$$

$$\int d\sigma_e\left[F(E - T_e, \theta, z) - \Delta z \frac{\partial F(E - T_e, \theta, z)}{\partial z}\right]\right] +$$

$$\left[1 - \frac{\Delta z N}{\cos \theta}(\int d\sigma_n + \int d\sigma_e)\right]\left[F(E,\theta,z) - \Delta z \frac{\partial F(E,\theta,z)}{\partial z}\right] \quad (A3)$$

Rearranging terms and letting $\Delta z \to 0$ gives an integral

CONCLUSION

By solving the two-dimensional diffusion equation in cylindrical coordinates, the distribution of sputtered neutral sample atoms in a GD system can be calculated. With the distribution the diffusional mass transport to different parts of the cell can then be estimated. Diffusion to the sample surface is not uniform, resulting in a convex erosion pattern of the sample. By manipulating the boundaries of the GD system, modifications in the cell geometry can be made to improve the performance of a GD as an analytical tool regarding both the erosion of the sample (depth profiling) and the sensitivity of a GD analysis.

The depth profiling abilities of a GD system are affected by the amount of material liberated into the plasma. Flatter crater profiles are theoretically obtained when less material is sputtered away. This can be achieved by lowering the discharge power but also by a partial shielding of the sample. The latter approach lowers the information thickness but still a relatively high etching rate can be maintained.

Using the calculated axial density profiles, it is shown that a more efficient transport of material toward the end of the cell can be accomplished by a simple cell boundary modifi-
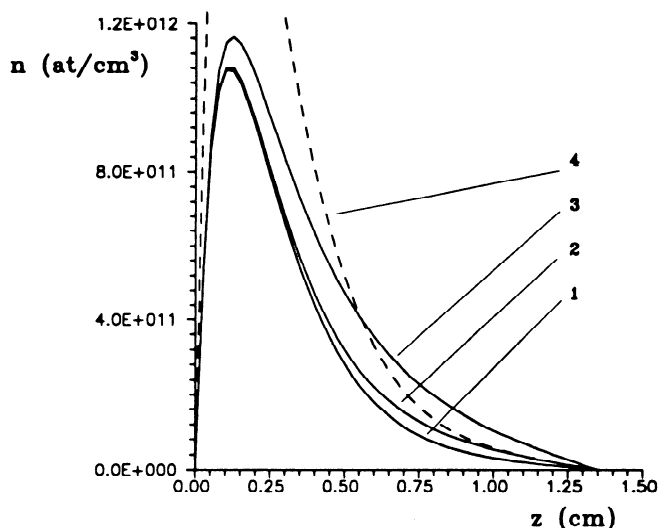
equation of the Boltzmann-type

$$-\cos\theta\,\frac{\partial F(E,\theta,z)}{\partial z} = N\int d\sigma_n[F(E,\theta,z) - F(E - T_n,\theta',z)] +$$
$$N\int d\sigma_e[F(E,\theta,z) - F(E - T_e,\theta,z)] \quad (A4)$$

Solving eq A4 is possible but laborious. Instead, a simplification can be made if one assumes a continuous slowing down (CSD) of the sputtered particles where scattering and inelastic collisions are neglected. This assumption gives realistic results for heavy sputtered particles with low energy slowing down in a gas environment of comparatively lighter atoms. With this approximation, eq A4 becomes

$$-\cos\theta\,\frac{\partial F(E,\theta,z)}{\partial z} = N\int d\sigma_n[F(E,\theta,z) - F(E - T_n,\theta',z)] \quad (A5)$$

Since only elastic collisions are taken into account, the second term of the right-hand side of eq A4 vanishes; θ' can be taken equal to θ for small scattering angles. Again expanding $F(E - T_n,\theta,z)$, assuming that T_n is small compared to E, but now up the first order in T_n gives

$$-\cos\theta\,\frac{\partial F(E,\theta,z)}{\partial z} = -N\int d\sigma_n T_n \frac{\partial F(E,\theta,z)}{\partial E}$$

$$= -N\frac{\partial F(E,\theta,z)}{\partial E}\int d\sigma_n T_n$$

$$= NS_n(E)\frac{\partial F(E,\theta,z)}{\partial E} \quad (A6)$$

where $S_n(E) = -\int d\sigma_n T_n$ is the nuclear stopping cross section. From eq A6 it follows that in the CSD approximation the position and energy of a stopping particle are simply related and all particles of a given energy and angle stop at the same point, producing a δ function distribution. The solution of eq A6 can then be written as

$$F(E,\theta,z) = \delta\left(z - \int_0^E \frac{dE}{NS_n(E)}\cos\theta\right) \quad (A7)$$

The nuclear stopping cross section can be related to the energy

(19) Johnson, R. E. Introduction to Atomic and Molecular Collisions; Plenum Press: New York, 1982.

loss of the particle slowing down along its straight line trajectory[19]

$$-\frac{dE}{ds} = NS_n(E) = N\int d\sigma_n T_n \quad (A8)$$

For inverse power law interaction potentials between the slowing down neutral and the target gas atoms ($V(r) \propto r^{-1/t}$) one can write

$$-\frac{dE}{ds} = \alpha E^{1-2t} \quad (A9)$$

where α is a parameter depending on the pressure, the temperature, and the mass ratio M_g/M_s;[9] t is dependent upon the energy of the stopping particle and is taken equal to $1/4$ here. Since the CSD model neglects scattering, transformation from the original direction to a direction along the source normal is straightforward:

$$-\frac{dE}{dz} = \frac{\alpha E^{1/2}}{\cos\theta} \quad (A10)$$

Combining eqs A10 and A7, the distribution of stopped particles is obtained:

$$F(E,\theta,z) = \delta\left(z - \int_0^E \frac{dE}{\alpha E^{1/2}}\cos\theta\right) \quad (A11)$$

The integral $\int_0^E dE/\alpha E^{1/2}$ corresponds to the range of a particle with initial energy E. Solving the integral in eq A11 and inserting the distribution of stopped particles in the convolution integral (eq 8) yields the required thermalization profile for the emitted particle flux:

$$F_T(z) = \int\int dE\,d\Omega\,\Phi(E,\theta)\,\delta(z - (\alpha/2)^{-1}E^{1/2}\cos\theta) \quad (A12)$$

This integral is analytically solvable; following ref 9, the thermalization profile then can be written as

$$F_T(z) = \frac{R_U/z}{(1 + (R_U/z)^2)^2} \quad (A13)$$

where $R_U = \int_0^U dE/\alpha E^{1/2}$ is the range of particles with energy U, the surface binding energy of the target.